Integrated multi-omics analysis reveals common and distinct dysregulated pathways for genetic subtypes of Frontotemporal Dementia

Kevin Menden[1,*] (KM); Margherita Francescatto[1] (MF); Tenzin Nyima[1] (TN); Cornelis Blauwendraat[1,2] (CB); Ashutosh Dhingra[1] (AD); Melissa Castillo-Lizardo[1] (MC); Noémia Fernandes[1] (NF); Lalit Kaurani[4] (LK); Deborah Kronenberg-Versteeg[1,3] (DKV); Burcu Atarsu[1,3] (BA); Eldem Sadikoglou[1] (ES); Barbara Borroni[6] (BB); Salvador Rodriguez-Nieto[1] (SRN); Javier Simon-Sanchez[1,3] (JSS); Andre Fischer[4] (AF); David Wesley Craig[7] (DWC); Manuela Neumann[1] (MN); Stefan Bonn[1,5] (SB); Patrizia Rizzu[1] (PR); Peter Heutink[1,*] (PH).

Affiliations

1 German Center for Neurodegenerative Diseases, Tübingen, Germany

2 National Institute on Aging, National Institutes of Health, Bethesda, MD, USA

3 Hertie Institute for Clinical Brain Research, Tübingen, Germany

19 4 German Center for Neurodegenerative Diseases, Göttingen, Germany

20 5 Institute of Medical Systems Biology, University Medical Center Hamburg-Eppendorf,
21 Hamburg, Germany

22 6 Neurology Unit, Department of Clinical and Experimental Sciences, University of Brescia,
23 Italy

24 7 University of Southern California, California, USA

25

26 * corresponding authors

27 Peter Heutink: peter.heutink@dzne.de

28 Kevin Menden: kevin.menden@qbic.uni-tuebingen.de

29

30 Abstract

31 Understanding the molecular mechanisms underlying frontotemporal dementia (FTD) is
32 essential for the development of successful therapies. Here we integrated transcriptomic and
33 epigenomic analyses of postmortem human brains of FTD patients with mutations in MAPT,
34 GRN and C9orf72 and detected common and distinct dysregulated cellular pathways
35 between patient groups. Our results highlight that excitatory neurons are the most vulnerable
36 neuronal cell type and that vascular aberrations are a common hallmark in FTD. Via
37 integration of multi-omics data, we detected several transcription factors and pathways
38 which regulate the strong neuroinflammation observed in FTD-GRN. Small RNA-seq data
39 and verification experiments in cellular models identified up-regulated miRNAs that inhibit
40 cellular trafficking pathways in FTD and lead to microglial activation. These findings shed
41 light on novel mechanistic and pathophysiological hallmarks of FTD. The data represent the

1st phase of a multi-omics, multi-model data resource for FTD research which allows in-depth molecular research into disease mechanisms that will further mechanistic FTD research.

Introduction

Frontotemporal Dementia (FTD) is a devastating pre-senile dementia characterized by progressive deterioration of the frontal and anterior temporal lobes [1]. The most common symptoms include severe changes in social and personal behaviour as well as a general blunting of emotions. Clinically, genetically, and pathologically there is considerable overlap with other neurodegenerative diseases including Amyotrophic Lateral Sclerosis (ALS), Progressive Supranuclear Palsy (PSP) and Cortical Basal Degeneration (CBD) [2]. Research into FTD has made major advances over the past decades. Up to 40% of cases [3] have a positive family history and up to 60% of familial cases can be explained by mutations in the genes Microtubule Associated Protein Tau (MAPT), Granulin (GRN) and C9orf72 [4] which has been key to the progress in our understanding of its molecular basis. Several other disease-causing genes have been identified that account for a much smaller fraction of cases [5]. Mutations in MAPT lead to accumulation of the Tau protein in neurofibrillary tangles in the brain of patients while mutations in GRN and C9orf72 lead to the accumulation of TDP-43 [6], as well as dipeptide repeat proteins (DPRs) and RNA foci in the case of C9orf72 [7].

As of today, no therapy exists that halts or slows the neurodegenerative process of FTD and in order to develop successful therapies there is an urgent need to determine whether a common target and therapy can be identified that can be exploited for all patients, or whether the distinct genetic, clinical and pathological subgroups need tailored treatments. Therefore, the development of remedies relies heavily on a better understanding of the molecular and cellular pathways that drive FTD pathogenesis in all FTD subtypes.

67 Although our knowledge of FTD pathogenesis using molecular and cellular biology
68 approaches has significantly advanced during recent years, a deep mechanistic
69 understanding of the pathological pathways requires simultaneous profiling of multiple
70 regulatory mechanisms. As neurodegenerative diseases develop over time, it is furthermore
71 important to examine temporal changes. While post-mortem human brain tissue represents
72 the end-stage of disease, well-defined rodent models can be used to address the temporal
73 component. Lastly, experimental validation of derived hypotheses can be achieved in cellular
74 systems, such as neurons derived from induced pluripotent stem cells (iPSCs) as well as in
75 rodent models.

76 The Risk and modifying factors in Frontotemporal Dementia (RiMod-FTD) consortium[8]
77 generates a multi-model and multi-omics data resource with the focus on mutations in the
78 three most common causal genes: MAPT, GRN and C9orf72. The data resource will consist
79 of multi-omics datasets from multiple post-mortem human brain regions, and matching iPSC
80 derived neurons and brain tissue of transgenic mouse models at different time points.

81 Here, we report on data derived from the post-mortem human brain RNA-seq, CAGE-seq,
82 smRNA-seq and methylation datasets from RiMod-FTD. We identified dysregulation of
83 overlapping pathways in all disease groups that indicates converging disease mechanisms
84 manifesting during disease progression. Using deconvolution analysis, we have identified
85 changes in cellular composition that are either common or distinct to genetic subgroups.
86 Through integration of smRNA-seq and CAGE-seq data, we could furthermore highlight
87 potential regulatory molecules that might play important roles in FTD pathogenesis, within
88 the identified functional gene modules and pathways.

Results

Multi-omics Data Resource for Frontotemporal Dementia

We have analysed data from brain tissue from diseased patients carrying mutations in the MAPT (n=17), GRN (n=11) or C9orf72 (n=17) genes and non-demented controls (n=16). The average age of FTD groups was lower than that of healthy controls (Table S1). We obtained tissue from up to 7 regions for each brain. The temporal and frontal lobes are the most affected areas in FTD, but we also obtained material from the occipital lobe, hippocampus, caudate, putamen and cerebellum for verification experiments. We performed CAGE-seq, smRNA-seq and quantitative proteomics (Miedema et al., manuscript in preparation) on tissue from frontal and temporal lobes, and generated methylation and RNA-seq data for frontal lobe tissue. Additional data types such as ATAC-seq, transgenic mouse models and iPS derived data are planned for future releases. The resulting, comprehensive multi-omics data resource enables the study of disease mechanisms in FTD subtypes to greater detail than single genomics experiments (Fig. 1).

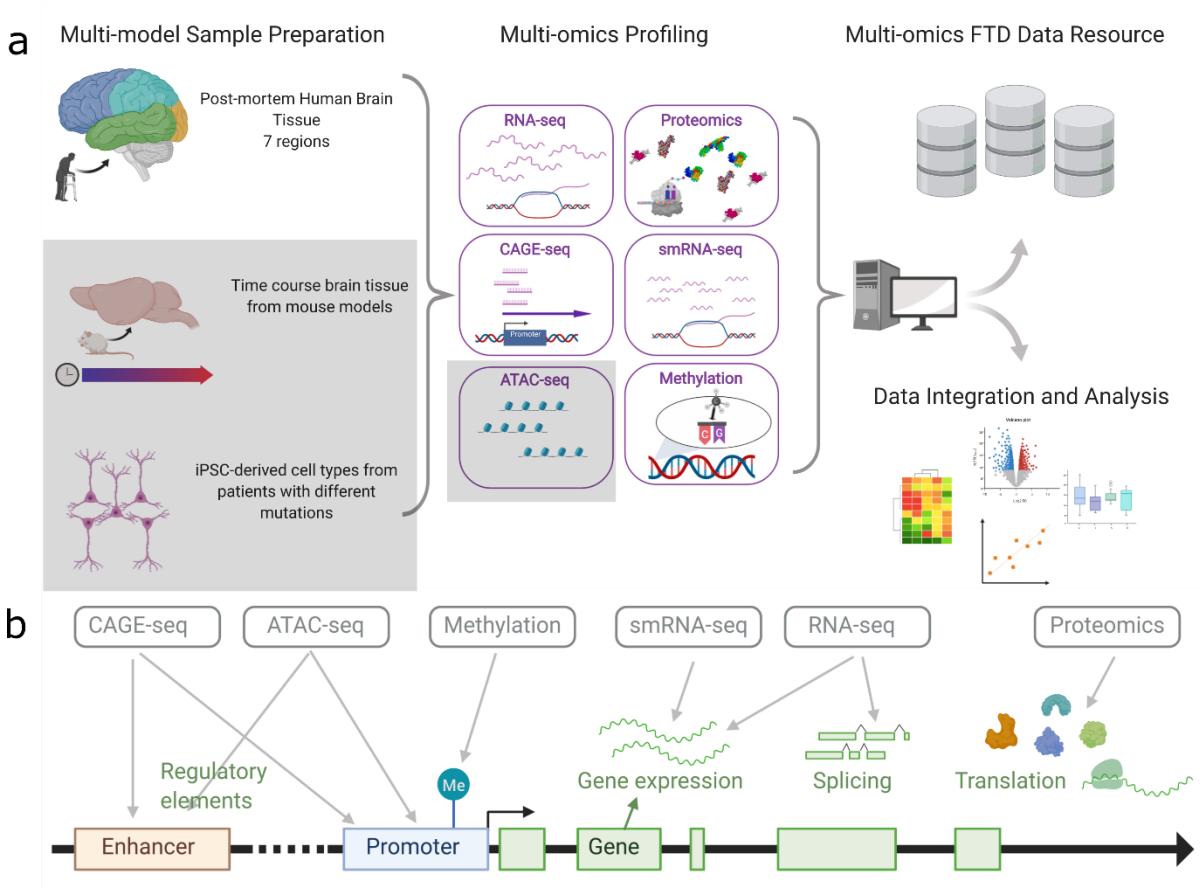

Figure 1: Graphical overview of the RiMod-FTD project. a In phase 1, Human Post-mortem brain tissue samples from multiple regions of patients with mutations in GRN, MAPT and C9orf72 have been collected and used for multi-omics data generation. Grey shading indicates datasets that will be completed in future phases. The datasets have been integrated and analysed and published to be accessible as FTD resource. In subsequent phases additional datatypes will be added (i.e. ATAC-seq) and the resource will be extended with data from matching mouse models and iPSC derived celltypes. **b** The multi-omics approach allows to profile multiple regulatory features of gene expression, including enhancer- and promoter-based regulation, epigenetic regulation, alternative splicing, post-transcriptional regulation (miRNAs) and regulation of translation (proteomics).

116 In the current study, we have integrated RNA-seq, CAGE-seq, smRNA-seq and methylation
117 data from the Gyrus Frontalis Medialis (GFM) (Table S2), as this brain region is strongly
118 affected in FTD.

119

120 Differential gene expression analysis and cellular deconvolution
121 of the GFM in FTD.

122 To identify general gene expression patterns in the GFM of patients with FTD, we performed
123 differential gene expression (DGE) and principal component analysis (PCA) using RNA-seq
124 data. The PCA indicates considerable heterogeneity between samples, as can be expected
125 from post-mortem human brain tissue (Fig. 2a). However, a difference between FTD cases
126 and control samples is clearly visible. Differentially expressed genes (DEGs) were calculated
127 for all disease groups (FTD-MAPT, FTD-GRN, FTD-C9orf72) compared to controls while
128 controlling for gender and pH-value (see Methods). We observed the largest number of
129 DEGs (adj. P-value < 0.05) for FTD-GRN, followed by FTD-MAPT and FTD-C9orf72 (Fig.
130 2b). DGE of smRNA-seq data yielded 78, 21 and 39 differentially expressed miRNAs in
131 FTD-MAPT, FTD-GRN and FTD-C9orf72, respectively (Fig. 2c).

132

133 Due to the neurodegenerative nature of FTD, it is likely that there exists a systematic
134 difference in cell composition between cases and controls which can affect DGE analysis
135 due to differences in gene expression between cell types - a problem which has often been
136 overlooked in tissue expression studies. Here, we account for this problem by applying a
137 conservative filtering approach and removing DEGs that are associated with changing
138 cellular composition (see Methods). All further analyses were based on the filtered set of
139 DEGs, unless otherwise specified. Note that this method could only be applied to the total

140 RNA-seq dataset because similar cell type specificity data (here, single-cell RNA-seq data)
141 was not available for other data types.

142

143 Activation of extracellular matrix (ECM) associated pathways
144 and circulatory system development.

145 We next performed pathway enrichment analysis with DEGs from the RNA-seq data using
146 go:Profiler[9] to identify the most affected cellular pathways. Down-regulated genes are
147 strongly enriched for mitochondrial and oxidative phosphorylation pathways in both FTD-
148 GRN and FTD-MAPT (Fig. 2d, Fig. S1), indicating a dysfunctional energy metabolism - a
149 well-known hallmark of many neurodegenerative diseases[10]. Neuronal system pathways are
150 enriched among down-regulated genes for both groups as well. This might be explained by
151 dysfunctional neurons that have not yet undergone apoptosis or by a general impairment of
152 neuronal function caused by the disease. Other significantly down-regulated pathways
153 include ubiquitin-dependent protein metabolism and vesicle-mediated transport (FTD-GRN).
154 In all three groups, up-regulated genes are enriched for extracellular matrix (ECM)
155 associated pathways and circulatory system development (Fig. S1). Genes involved in
156 Hippo-signalling are enriched in FTD-GRN and FTD-MAPT (Fig. 2d), and immune system
157 related genes are enriched in FTD-GRN. ECM dysregulation, in particular, has been
158 implicated with several neurodegenerative diseases. For instance, studies in mouse models
159 showed that tau pathology can lead to ECM reorganization and that reducing ECM proteins
160 could reverse memory deficits in an AD model[11,12]. While the role of the ECM in FTD
161 remains unknown, our results suggest a prominent involvement in end-stage FTD.

162

163 We also specifically examined the DEGs with the largest fold-changes in the RNA-seq data
164 because large expression fold-changes often signify strong dysregulation. These results

support the importance of ECM in FTD as for all disease groups, multiple matrix metalloproteinase enzymes (MMPs) are among the DEGs with the largest LFCs (Fig. S2, Fig. S3A). Elevated RNA levels of MMP genes have been reported for many neurodegenerative diseases, and MMPs target a wide range of ECM [13]indicating their importance in neurodegenerative mechanisms[14]. Protein interaction networks of up-regulated genes in FTD-MAPT and FTD-GRN show the central importance of MMPs in these networks (Fig. S3 B & C).

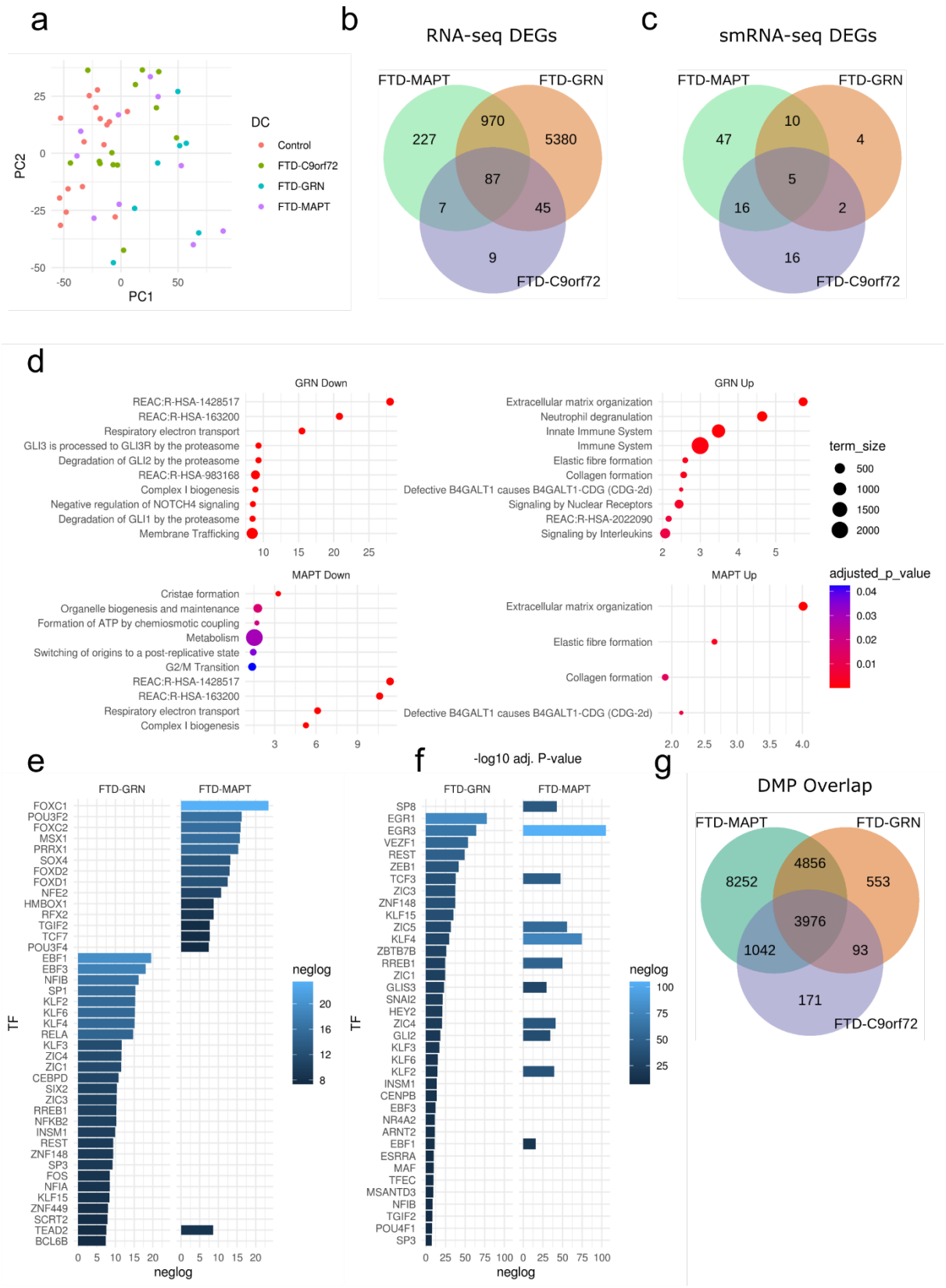

174

175 **Figure 2**: **Gene- and Pathway-level transcriptional changes in FTD. a** Principal

176 component analysis of variance stabilized RNA-seq expression values, coloured by group. **b**

177 Overlap between RNA-seq DEGs from different disease groups. **c** Overlap between
178 smRNA-seq DEGs from different disease groups. **d** Enriched Reactome pathways in RNA-
179 seq up- and down-regulated DEGs. Shown are the ten most significant pathways per group;
180 the x-axis signifies the negative log10 P-value. Colour corresponds to adjusted P-value and
181 node size corresponds to the number of genes in a pathway. **e,f** Best candidates for active
182 and inactive TFs in FTD-GRN and FTD-MAPT, respectively. The x-axis signifies the
183 negative log10 P-value. **g** Overlap of DMPs in different disease groups.

184

185 Regulatory mechanisms associated with differential expression

186 To better understand relevant regulatory mechanisms leading to these gene expression
187 changes, we generated a set of candidate driver transcription factors (TFs) using the GFM
188 CAGE-seq data. CAGE-seq cluster counts, when assigned to the closest gene, correlate
189 well with RNA-seq expression data (average sample-wise correlation coefficient: 0.6, Fig.
190 S4). We used the CAGE-seq data to predict candidate driver TFs for up- and down-
191 regulated genes (see Methods for details). TEAD2, a TF central to the Hippo signalling
192 pathway, is the only predicted active TF common to FTD-GRN and FTD-MAPT (Fig. 2e),
193 while there is greater overlap among inactive TFs (here: inactive TF = has down-regulated
194 targets, Fig. 2f). Moreover, we performed miRNA-target gene mapping to evaluate potential
195 regulatory roles of miRNAs. Expression values of miRNAs were correlated with their
196 predicted targets using matching samples from the RNA-seq data. Only miRNA-target pairs
197 with considerable negative correlation were retained (see Methods).

198

199 DNA methylation is another important regulatory mechanism that can affect gene
200 expression. We generated Illumina Infinium EPIC methylation data from the GFM and
201 considered the most variable CpG sites (28,173) corrected for possible confounding effects

202 using surrogate variable analysis (SVA) to perform differential methylation analysis (see
203 Methods). We detected 18,126, 9,478 and 5,282 significantly differentially methylated
204 positions (DMPs) for FTD-MAPT, FTD-GRN, and FTD-C9orf72, respectively (Fig. 2g). The
205 C9orf72 repeat expansion is known to be associated with hypermethylation[15] and we
206 confirmed in our data that a CpG site located at the 5'-end of the C9orf72 gene, only 14 bp
207 away from the repeat expansion, is hypermethylated (log fold-change: 0.6, Fig. S4A).
208 Pathway enrichment analysis of genes in proximity to DMPs yielded enrichment of genes
209 involved in nervous system development for hypermethylated CpG sites. Genes close to
210 hypomethylated sites were enriched for system development and vasculature development
211 (Fig. S5C). As hypermethylation of CpG sites at promoter regions is associated with
212 decreased expression, this indicates epigenetically controlled expression inhibition of genes
213 important for neuronal function, or remnants of cell composition effects that could not be
214 entirely alleviated by SVA (see Methods). Performing biological age prediction using the
215 methylation data resulted in underestimated age predictions for all groups, albeit to a lesser
216 extent for FTD groups, which indicates accelerated aging in FTD (Fig. S5B).

217 Vulnerability of excitatory neurons and enrichment of 218 endothelial cells

219 To identify vulnerable cell types and disease-related cell composition changes, we inspected
220 the results from the RNA-seq deconvolution analysis (Methods) with respect to genetic FTD
221 subtypes. As expected, fractions of neuronal cells are systematically lower in all FTD groups
222 compared to controls (Fig. S6). Consequently, virtually all other cell types show increasing
223 percentages. We therefore calculated the percentage-wise change for each cell type and
224 assessed statistical significance (see Methods). Strongest neuronal loss was observed in
225 FTD-GRN, followed by FTD-MAPT and FTD-C9orf72 (Fig. 3a, Table S3), which agrees with
226 studies that have shown that the frontal lobe is most strongly affected in FTD-GRN[16–18].
227 Moreover, neuronal loss can be primarily attributed to loss of excitatory neurons, while

228 fractions of inhibitory are not significantly different to controls (Table S3). Our results confirm
229 findings from recent studies that found excitatory neurons to be especially vulnerable to tau
230 pathology[19] and we specifically detected an important role of glutamatergic
231 neurotransmission in FTD [20,21]. Closer examination of the KEGG pathway 'glutamatergic
232 synapse' suggests that AMPA receptors are mainly affected, while we could not see signs of
233 dysregulation for NMDA receptors (Fig. S7 A-C). Analysis of candidate regulator TFs
234 highlighted the TF Early Growth Response 3 (EGR3), targets of which are enriched for
235 glutamatergic synapse genes (Fig. S7D), indicating involvement in excitatory neuronal
236 function.

237

238 To validate our computational deconvolution, we considered the fractions of excitatory
239 neurons as a proxy of neurodegeneration and correlated them with manually determined
240 degeneration scores by a neuropathologist (Fig. 3b, Methods). Indeed, excitatory neuron
241 fractions show strong negative correlation with pathology scores (Pearson's correlation
242 coefficient = -0.78, P-value = 2.8e-07), thereby providing experimental confirmation of our
243 computational predictions.

244

245 The strongest growth in percentage compared to the baseline is observed for endothelial
246 cells in FTD-MAPT and FTD-C9orf72 disease groups, but not FTD-GRN, where microglial
247 cells show the strongest increase. Circulatory system development is among the most
248 significantly up-regulated biological processes in all three disease groups (Fig. 3 c & d). The
249 role of the circulatory system in FTD is relatively unexplored. However, Bennet et al. recently
250 found increased vasculature growth in mouse models of FTD-MAPT with a P301L
251 mutation[22]. Interestingly, endothelial enrichment in FTD-MAPT is particularly strong in
252 patients with a P301L mutation (Fig. 3a). Another recent study observed a particular
253 microvascular structure with increased frequency in brains of patients with frontotemporal

254 lobar degeneration (FTLD)[23] and Park et al. have shown that soluble tau can interfere with

255 nitric oxide production and thus lead to reduced vasodilation of blood vessels, ultimately

256 leading to insufficient blood supply [24].

257

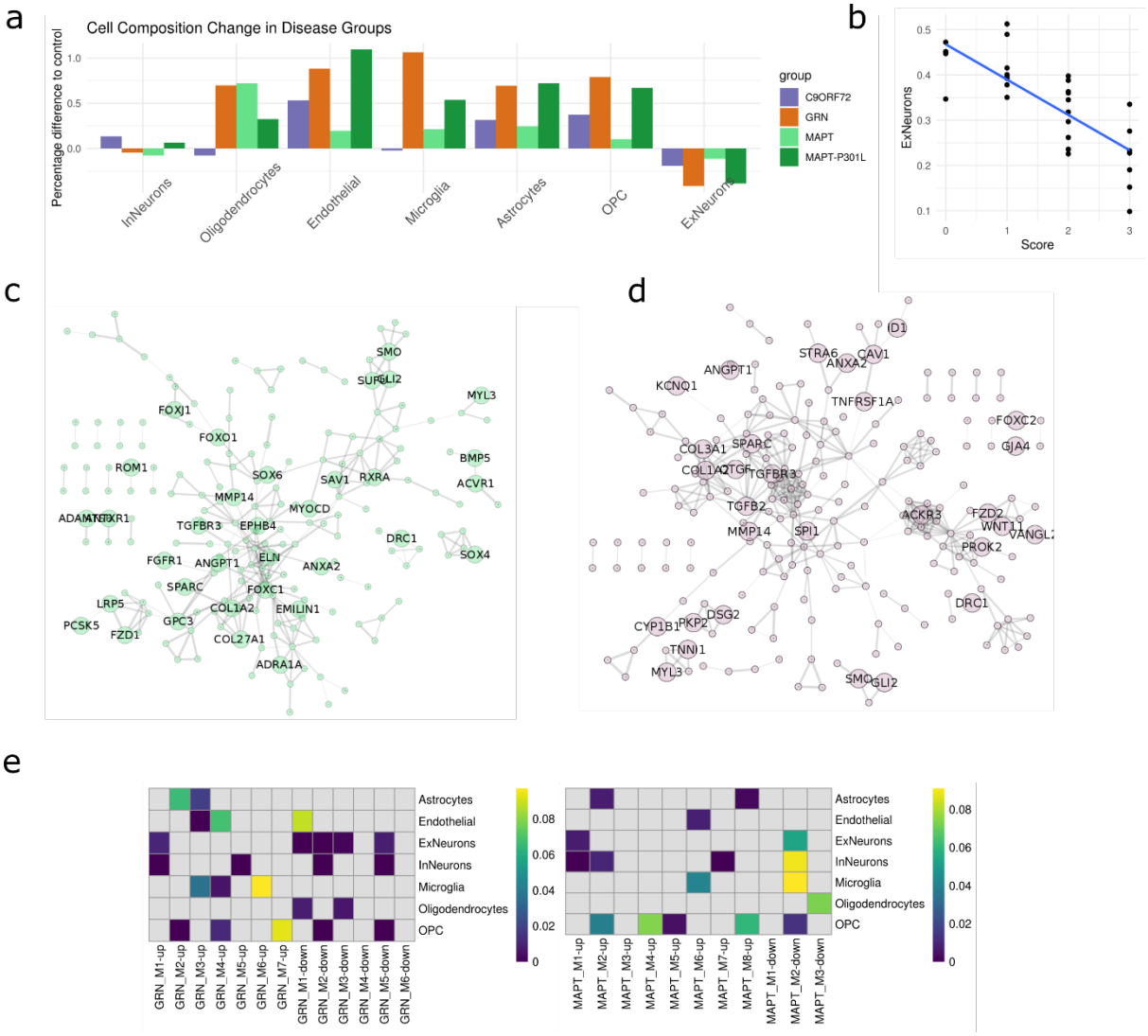

258

259 **Figure 3: Cell composition changes in FTD. a** Percentage change of averaged fractions

260 per group compared to the average of the control group. Genetic subtypes are indicated with

261 different colours. **b** Regression of excitatory neuron fractions (y-axis) against neuropathology

262 scores (x-axis). **c**, **d** PPI networks of genes up-regulated in FTD-MAPT and FTD-GRN (log-

263 fold-change > 1), respectively. Genes involved in the biological process “circulatory system

264 development” are labelled. **e** Heatmap of EWCE analysis results for HumanBase modules of

265 FTD-GRN and FTD-MAPT. Different modules are lined up on the x-axis, different cell types
266 on the y-axis. Tile colour signifies the EWCE P-value. Tiles with P-values above 0.1 are
267 marked grey.

268

269

270 To better understand transcriptional changes and regulatory mechanisms, we performed
271 tissue-specific functional module detection with HumanBase[25] and assessed cell type
272 specificity of modules using EWCE[26]. Both for FTD-MAPT and FTD-GRN, most modules
273 show specificity for a few cell types (Fig. 3e). Up-regulated modules in both groups are
274 significantly enriched for endothelial genes (P-value < 0.1). Genes within these modules
275 have been associated with blood vessel development (FTD-MAPT M6-up) and endothelial
276 cell growth (FTD-GRN M4-up) by HumanBase (Fig. 3 c & d), further supporting a distinct
277 involvement of endothelial genes in these FTD subtypes.

278

279 Increased Inflammatory response in FTD-GRN

280 In patients with FTD-GRN, microglial fractions show an even larger relative increase than
281 endothelial cells, indicating increased microglial activity. The protein encoded by GRN is well
282 known for its importance to lysosomal function, is highly expressed in microglia and well-
283 known for having important functions in the immune system [27,28]. Microglia are also slightly
284 enriched in FTD-MAPT (P-value = 0.037) but not in FTD-C9orf72 (P-value = 0.475).

285 Here, we have observed a prominent increase in microglial cell fractions and up-regulation of
286 immune system pathways in FTD-GRN, a feature of GRN deficiency that has been
287 frequently shown in mouse models[28–30]. We therefore wanted to further characterize
288 potential underlying regulatory mechanisms. First, we examined FTD-GRN modules for
289 enrichment of immune system-related terms. Indeed, several up-regulated modules are

290 enriched for genes related to the immune system, while we could not find enrichment among
291 down-regulated modules. The module FTD-GRN M1-up contains genes important for
292 neutrophil migration and response to interleukins (Fig. 4 a & d). Both modules M3-up and
293 M4-up contain genes relevant to NF-kappa-B (NFkB) signalling, as well as genes involved in
294 tumour necrosis factor (TNF) production (Fig. 4 b & c, respectively). Finally, the module M6-
295 up is enriched for genes involved in T cell activation. Modules M3-up, M4-up and M6-up are
296 furthermore enriched for microglial-specific genes (Fig. 3e). Interestingly, several
297 necroptosis-related genes are up-regulated (M1-up: TLR3, TLR8, RIPK3; M4-up: RIPK2),
298 suggesting this pathway as a potential driver of neuronal death. While we did not detect
299 prominent signals for neuroinflammation in FTD-MAPT, the FTD-MAPT module M3-up
300 contains several genes involved in T cell and TNF signalling (EZR, RAB29, CARD8, HIPK1).
301 However, neuroinflammation is much less prominent in FTD-MAPT and FTD-C9orf72
302 compared to FTD-GRN.

303

304

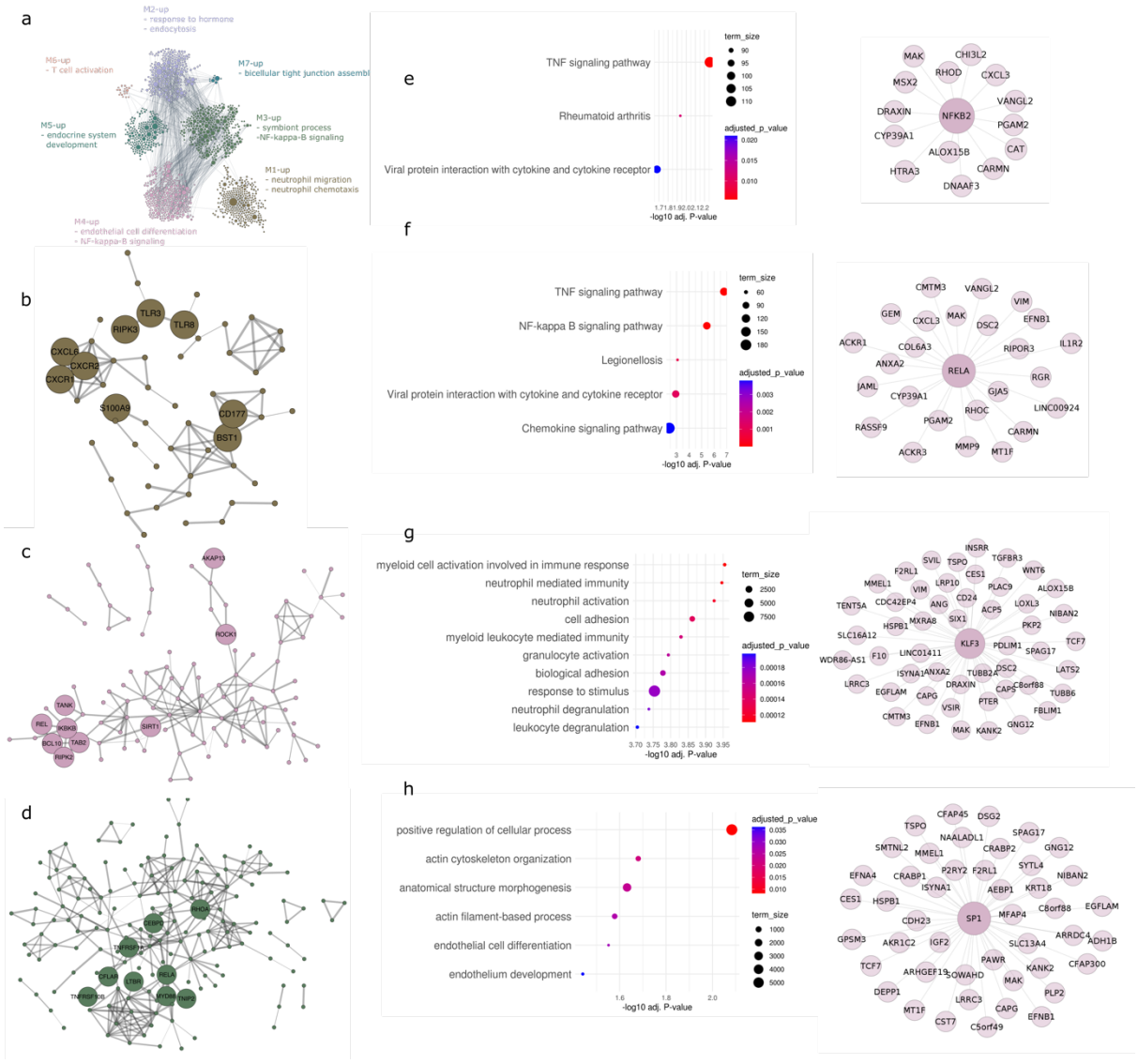

Figure 4: **Neuroinflammation in FTD-GRN. a** Up-regulated HumanBase modules in FTD-GRN with most significant terms. **b** Protein-protein interaction (PPI) network (made with String-DB) of FTD-GRN M1 up-module. Genes involved in necroptosis, interleukin response and neutrophil migration are indicated **c** PPI network of FTD-GRN M4-up module. Genes involved in NFkB signalling are indicated. **d** PPI network of FTD-GRN M3-up module. Genes involved in NFkB signalling and CEPBD are indicated. **e** and **f** KEGG pathway enrichment of predicted targets of TFs NFKB2 and RELA, respectively. **g** and **h** GO:BP pathway enrichment of predicted targets of TFs KLF3 and SP1, respectively.

315

316 Inspection of our candidate regulator TFs indicated the TFs Nuclear Factor Kappa B Subunit
317 2 (NFKB2) and RELA which together form the NFkB signalling complex, as potential drivers
318 in FTD-GRN (Fig. 2e). Enrichment analysis of predicted NFKB2 and RELA targets in FTD-
319 GRN indeed revealed TNF signalling and NFkB signalling as the most significantly enriched
320 KEGG pathways (Fig. 4 e & f). Furthermore, enrichment analysis indicated targets of the TFs
321 SP1 and KLF3 as highly enriched among genes in the FTD-GRN M3-up module. Predicted
322 KLF3 targets are enriched for immune system genes (Fig. 4g). SP1 target genes do not
323 show a strong enrichment but have roles in actin cytoskeleton organization and endothelial
324 cell differentiation, among others (Fig. 4h). We also investigated predicted targets of down-
325 regulated miRNAs and genes proximal to hypomethylated CpG sites for involvement in the
326 immune system in FTD-GRN but could not detect any significant immune system-relevant
327 enrichment suggesting they do not play a major role in regulating the immune response.

328

329 To closer examine which parts of the NFkB and TNF signalling pathways are affected in
330 FTD-GRN and in FTD in general, we inspected fold-changes of genes from the
331 corresponding KEGG pathways. Interestingly, the pro-inflammatory cytokine Interleukin 1
332 Beta (IL1B) is down-regulated in all disease groups, although only significantly in FTD-MAPT
333 (Fig. S9A). Similarly, the inflammatory cytokine Interleukin 6 (IL6) has negative fold-changes
334 in all disease groups. Downstream effector genes with positive fold-changes include multiple
335 chemokines, Interleukin 18 Receptor 1 (IL18R1) and several metalloproteinases.

336

337 GRN deficiency in mouse models leads to overactivation of microglia[28] and GRN deficiency
338 leads to NFkB overactivation in microglia in a GRN loss-of-function mouse model[29].
339 Hyperactivation of TNF by NFkB signalling has been linked to obsessive-compulsive

340 behaviour (OCB) and inhibition of NFkB was sufficient to rescue the behavioural symptoms
341 linking these TFs to the OCB observed in patients.

342 Dysfunctional energy metabolism and cellular trafficking in FTD

343 Among the most significantly down-regulated pathways in FTD-GRN and FTD-MAPT are
344 several pathways involved in energy metabolism and oxidative phosphorylation (Fig. 2d, Fig.
345 S1). Inspection revealed the modules FTD-GRN M1-down and FTD-MAPT M1-down as
346 being most significantly associated with the term NADH dehydrogenase complex assembly
347 (Fig. 5 d & e, Tables S4 and S5). Further inspection of the FTD-MAPT and FTD-GRN M1-up
348 modules revealed that they contain several NADH:Ubiquinone Oxidoreductase Subunit
349 genes (Fig. 5 b & c), which are necessary for functional oxidative phosphorylation and hence
350 energy production. The FTD-GRN module is moreover enriched for genes involved in
351 intracellular transport and autophagy. The FTD-GRN M1-down module contains several
352 genes associated with FTD or ALS: Superoxide Dismutase 1 (SOD1), Dynactin Subunit 1
353 (DCTN1), PTEN Induced Kinase 1 (PINK1), Huntingtin (HTT), and CHCHD10. All these
354 genes show lower expression values in every genetic subgroup, although they do not reach
355 significant levels in all groups (Fig. 5a).

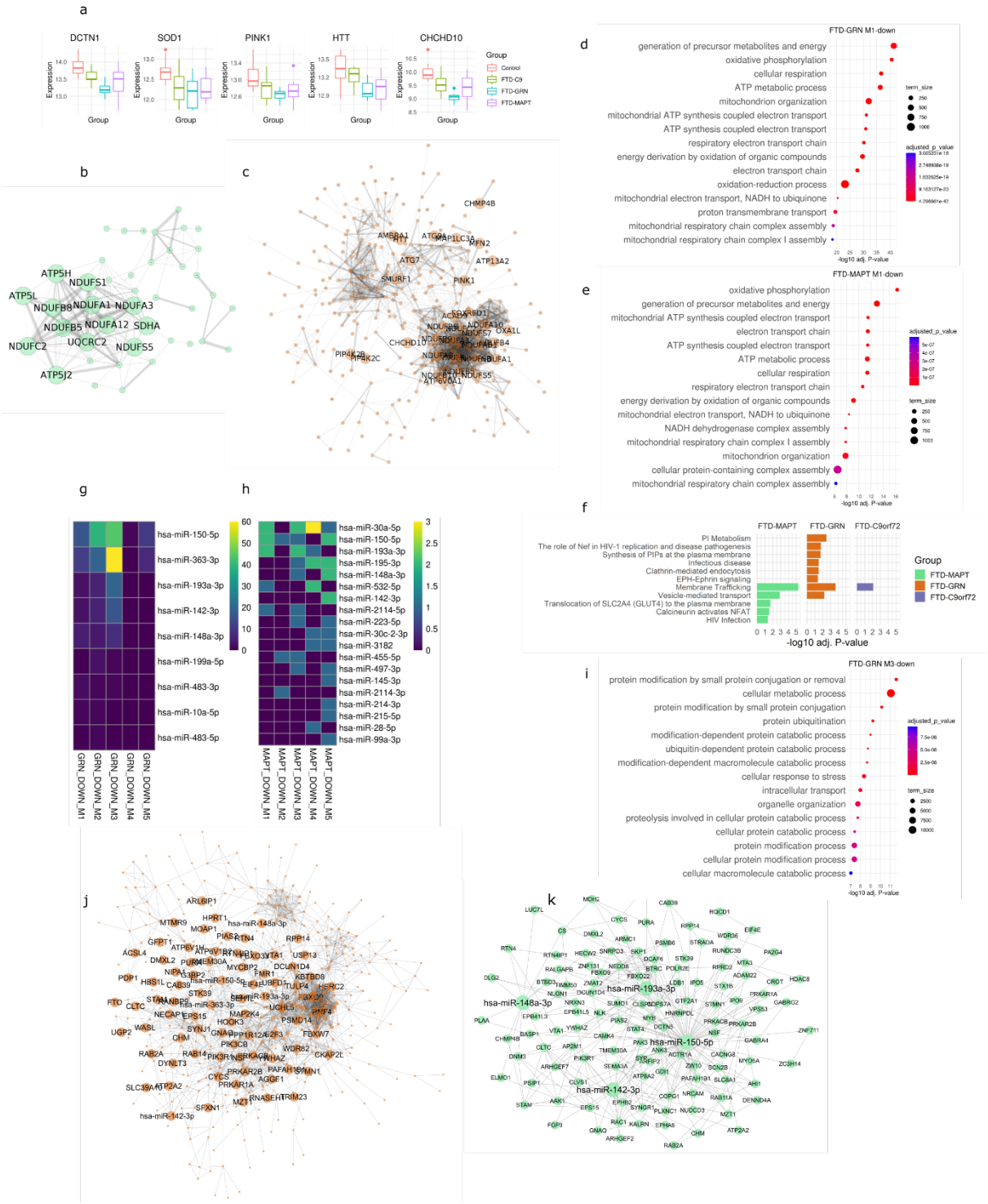

-

Figure 5: Impaired oxidative phosphorylation and cellular trafficking in FTD. a Expression levels (variance stabilized with DESeq2) of the genes CHCHD10, PINK1, SOD1, DCTN1 and HTT in different groups. **b** STRING-DB PPI of FTD-MAPT M1-down module. Genes involved in oxidative phosphorylation are labelled. **c** PPI of FTD-GRN M1-down

362 module. Genes involved in NADH dehydrogenase complex assembly and mitophagy are
363 labelled, as well as CHCHD10. **d, e** Most significant results from pathway enrichment
364 analysis with g:Profiler (GO biological process) for the FTD-GRN M1-down module and the
365 FTD-MAPT M1-down module, respectively. Node colour corresponds to adjusted P-value
366 and node size to term size. **f** Most significant results from enrichment analysis (Reactome) of
367 targets of up-regulated miRNAs in all disease groups. **g, h** Heatmaps of intersection-over-
368 union scores between predicted miRNA targets and down-regulated modules in FTD-GRN
369 and FTD-MAPT, respectively. **i** Top enrichment results of g:Profiler (GO biological process)
370 for the FTD-GRN M3-down module. Node colour corresponds to adjusted P-value and node
371 size to term size. **j** PPI network (String-DB) of FTD-GRN M3-down module. Predicted targets
372 of up-regulated miRNAs are labelled. **k** PPI network of predicted targets of up-regulated
373 miRNAs in FTD-MAPT.

374

375 Cellular transport is thought to play a key role in FTD pathogenesis as impaired trafficking
376 can affect protein and mitochondria homeostasis. Here, we show that mitochondrial function
377 is strongly impaired in end-stage FTD and that transport pathways are tightly connected to
378 this pathology. We thus looked for potential regulatory mechanisms driving the pathological
379 changes. Enrichment analysis of targets of up-regulated miRNAs in all disease groups
380 revealed cellular localization as the most significantly enriched biological process (GO:BP)
381 and membrane trafficking as the most significant Reactome pathway (Fig. 5f). Up-regulated
382 miRNAs in FTD therefore seem to primarily target cellular transport pathways and might play
383 important roles in dysfunctional transportation.

384

385 To detect modules and genes predominantly targeted by up-regulated miRNAs, we
386 calculated the intersection-over-union (IoU) of up-regulated miRNA targets with down-
387 regulated modules for FTD-GRN and FTD-MAPT (Fig. 5 g & h). The FTD-GRN M3-down

388 module is most strongly targeted by miRNAs and contains genes involved in metabolic
389 processes and cellular localization (Fig. 5i, Table S4). Five miRNAs have putative target
390 genes in this module: hsa-miR-150-5p, hsa-miR-142-3p, hsa-miR-193a-3p, hsa-miR-148a-
391 3p and hsa-miR-363-3p, which are all significantly up-regulated in FTD-MAPT as well,
392 except hsa-miR-363-3p. We generated networks of the above-mentioned candidate miRNAs
393 combined with a PPI network of the FTD-GRN M3-down module (Fig. 5j) and a PPI network
394 of all predicted targets in FTD-MAPT (Fig. 5k), as we could not detect a similar module in
395 FTD-MAPT. In total, we observed 31 common putative miRNA targets in both networks.

396

397 Next, we selected hsa-miR-193a-3p, hsa-miR-150-5p and hsa-miR-19b-3p for further
398 characterization in iPSC models (Fig. 6a). The first two miRNAs are DE in all three disease
399 groups and have many targets among module genes (Fig. 5 j & k). The miRNA hsa-miR-
400 19b-3p is up-regulated in all disease groups, although it does not reach significance after
401 (FTD-MAPT and FTD-C9orf72) or before (FTD-GRN) multiple testing correction.
402 Nevertheless, down-regulated genes were predicted to be enriched for targets of hsa-miR-
403 19b-3p by g:Profiler, the miRNA is known to inhibit autophagy [31] and it is highly expressed in
404 neurons. We performed RNA-seq on iPSC-derived neurons and microglia (Methods) that
405 were transfected with miRNA mimics and inhibitors for the three selected miRNAs. Here, we
406 focused on the mimic experiments, as the mimics should in theory reproduce the effects of
407 miRNA overexpression. Inhibition and mimicking of miR-150-5p in neurons had only minor
408 effects in neurons, while in microglia, the miR-150-5p mimic had strong effects, leading to
409 237 down-regulated and 236 up-regulated DEGs, enriched for cellular transport and immune
410 system pathways of the latter and nervous system development of the former (Fig. 6b).
411 Inhibition of miR-150-5p had even stronger effects (3221 DEGs), indicating an important
412 function of this miRNA in microglia. Transfection of miR-193a-3p mimic and inhibitor only
413 resulted in significant expression changes in microglia, where the mimic had strong effects
414 with 1756 down-regulated and 1474 up-regulated genes. Up-regulated genes were enriched

415 of mitochondrial functions like oxidative phosphorylation, while down-regulated genes were
416 enriched for localization and vesicle-mediated transport pathways (Fig. 6c).

417 In neurons, the miR-19b-3p mimic resulted in 89 down- and 137 up-regulated DEGs
418 (inhibitor: 8 down-regulated, 31 up-regulated). Genes down-regulated by the mimic and up-
419 regulated in the inhibitor experiment are involved in neuronal system pathways, enriched for
420 miR-19b-3p targets and share 17 common genes, thus providing evidence for these genes
421 to be regulated by miR-19b-3p. In microglia, stronger effects of the miR-19b-3p mimic
422 compared to the inhibitor were observed (1518 compared to 608 DEGs). Genes down-
423 regulated by the miR-19b-3p mimic were enriched for catabolic processes, autophagy and
424 vesicle-mediated transport, up-regulated genes were enriched for cell cycle and immune
425 system related genes (Fig. 6d). These results provide strong evidence that hsa-miR-19b-3p
426 and hsa-miR-193a-3p indeed regulate cellular trafficking pathways. Furthermore, hsa-miR-
427 150-5p is important for microglia function and up-regulation could lead to immune system
428 activation.

429

430

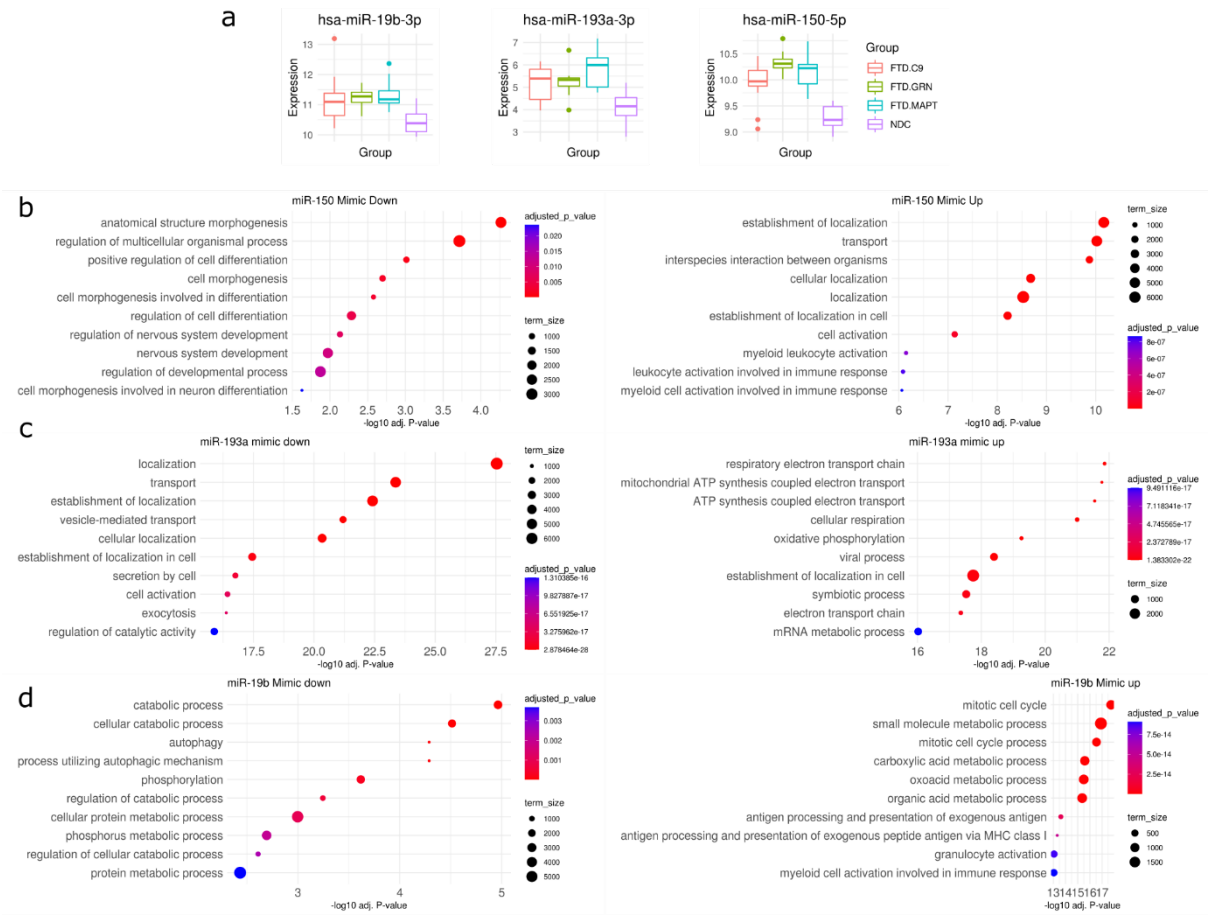

Figure 6: Effects of miRNA mimic and inhibitor experiments in iPSC-derived microglia. **a** Boxplots of normalized expression values for the selected miRNAs. **b**, **c**, **d** The top ten most significantly enriched biological processes of up- and down-regulated genes after transfection with mimics for miR-150-5p, miR-193a-3p and miR-19b-3p, respectively. Node size corresponds to the number of genes in the biological process term and node colour corresponds to the P-value adjusted for multiple testing.

Discussion

Here, we present the data from the 1st phase of the RiMod-FTD project, a multi-omics, multi-model data resource for FTD research that aims to understand the role of distinct genetic

443 risk factors in the disease. Generated by the RiMod-FTD consortium over several years, the
444 resource depicts a valuable tool for FTD researchers that will help to accelerate scientific
445 progress towards a better understanding of relevant disease mechanisms in FTD. Additional
446 multi-omics data from iPSC derived cell types, transgenic mouse models and other brain
447 regions will be added over time.

448

449 By studying post-mortem tissue of the GFM we detected the largest transcriptional
450 dysregulation and greatest neuronal loss in FTD caused by mutations in GRN, agreeing with
451 previous findings of a more pronounced frontal lobe atrophy in FTD-GRN compared to other
452 subtypes[32]. Our deconvolution analysis indicates that excitatory neurons are the most
453 affected cell type in all genetic subtypes of FTD, which was confirmed in the RiMod-FTD
454 proteomics data (Mediema et al., manuscript in preparation) as well. Recently, evidence
455 from multiple studies has accumulated pointing toward a strong involvement of glutamatergic
456 synapses in FTD[33]. While it has been previously reported that densities of both ionotropic
457 glutamate receptors, AMPA and NMDA receptors, are reduced in post-mortem brain tissue
458 of FTD patients[21], we see evidence that AMPA receptors are particularly affected.
459 Intriguingly, a recent single-nucleus RNA-seq study in a GRN mouse model could show that
460 hyperactivation of microglia leads to selective loss of excitatory neurons[34], which confirms
461 our hypothesis that excitatory neurons are especially vulnerable in FTD.

462 Strong neuroinflammation is a distinct feature of FTD-GRN, which is confirmed in our data
463 and by increased microglial cell numbers in this FTD sub-type, in line with recent findings
464 showing increased microglial burden in FTD-GRN[35,36]. Using an integrative approach, we
465 identified TFs: NFKB2, RELA, KLF3 and SP1 as key inflammatory drivers, leading to
466 activation of the NFkB- and TNF-signalling pathways.

467 We found indicators of activated necroptosis, suggesting this pathway as potential cause for
468 cell death. The necroptosis cell death pathway is deregulated in several neurodegenerative

469 disorders[37], and a recent study has shown that TBK1, a genetic cause of ALS and FTD (here
470 down-regulated in FTD-GRN), is an endogenous inhibitor of RIPK1, an upstream regulator of
471 RIPK3[38]. The authors showed that embryonic lethality of TBK1-knockout mice is dependent
472 on RIPK1 activity, suggesting that the necroptosis pathway is indeed an important player in
473 FTD pathogenesis. In a recent review, Molnár and colleagues have discussed several
474 available drugs that could potentially regulate necroptosis[39], highlighting the potential of this
475 pathway as a drug target for developing therapies for FTD.

476

477 Our pathway enrichment and deconvolution analyses pointed toward increased blood vessel
478 abundance and growth in FTD brains compared to controls, which is consistent with the
479 results from the RiMod-FTD proteomics data (Mediema et al., manuscript in preparation). It
480 is generally not known how and if the vasculature system is involved in FTD pathogenesis,
481 although recent studies have observed abnormalities in a mouse model of tau pathology and
482 post-mortem human brains[22,23]. To our knowledge, angiogenesis as a pathological feature in
483 several genetic FTD subtypes has not been reported before and therefore depicts an
484 important subject for FTD research.

485

486 In all three disease groups, we have observed prominent up-regulation of ECM pathways
487 and MMP enzymes, suggesting MMPs as important regulators in FTD pathogenesis. While it
488 has been increasingly recognized that MMPs are important regulators in many
489 neurodegenerative diseases [40,41], the role of MMPs in FTD pathogenesis has not been
490 investigated in depth. In mouse models of ALS, inhibition of the MMPs MMP2 and MMP9
491 could indeed prolong survival and reduce symptoms[42,43]. Moreover, TIMP3, which is up-
492 regulated in our data, was found to be partly responsible for neuronal apoptosis in an ALS
493 model [44], which points towards TIMP3 as a potential apoptosis mechanism in FTD. MMPs
494 are furthermore tightly involved in the inflammatory response, and can activate the tumour

495 necrosis factor (TNF) gene[45]. Inflammatory cytokines, hypoxia and reactive oxygen species
496 can lead to the activation of MMPs[40,46] and MMPs can digest the ECM, stimulate increased
497 production of growth factors and thereby promote the growth of blood vessels, providing a
498 potential causal link to the prominent enrichment of endothelial cells[46]. Given their important
499 biological functions and their involvement in all genetic FTD subgroups, it will be important to
500 further investigate how MMPs contribute to FTD and whether they can be exploited as drug
501 targets, as MMP inhibition in model system has shown promising results[47,48].

502

503 Impaired cellular trafficking mechanisms is very likely a key feature of FTD pathogenesis and
504 it has been shown multiple times that FTD-causal mutations lead to trafficking deficits [49–51].
505 However, it is not always clear which mechanisms continue to dysfunctional transport
506 mechanisms. Here, using multi-omics data and validation experiments, we show that
507 elevated expression of several miRNAs contributes to the inhibition of genes important for
508 cellular transport. Additional studies are necessary to further validate this hypothesis, which
509 directly suggests several miRNAs as putative drug targets.

510

511 While our study is reasonably powered, increasing the sample size for individual groups
512 such as FTD-C9orf72 would further increase the power of our analysis and help to better
513 define which pathways are truly distinct to certain subtypes. It will therefore be an objective
514 for future iterations of the RiMod-FTD resource to include larger numbers of samples.

515

516 To conclude, we present here an integrated multi-omics analysis on data from Phase 1 of
517 the RiMod-FTD project and developed new hypotheses on FTD disease mechanisms. The
518 data presented here highlights several regulator molecules important for FTD pathogenesis
519 and their consequences such as vascular abnormalities and thereby we show the value of
520 an integrated multi-omics data analysis for hypothesis generation and testing. The RiMod-

521 FTD data will be freely accessible to the scientific community through the European
522 Genome-phenome Archive (**EGA**) and a dedicated RiMod-FTD web application
523 (https://www.rimod-ftd.org) thus enabling scientists to derive new mechanisms and
524 hypotheses from the data.

525

526

527

528

529

530 Methods

531 **Donor samples employed in this study**

532 *Post mortem human brains*

533 Tissues were obtained under a Material Transfer Agreement from the Netherlands Brain
534 Bank, and additional samples were provided by the Queen Square Brain Bank of
535 Neurological Disorders and MRC, King College London. Demographic details about human
536 brain samples are summarized in Table S1.

537 GFM and GTM tissue from each subject was divided into three pieces for transcriptomic,
538 proteomic and epigenetic experiments in a dry-ice bath using precooled scalpels and
539 plasticware.

540

541 *hIPS-derived NGN2 neurons and miRNA mimics and inhibitors transfection*

542 smNPC were derived from hiPSc cells (Cell line id: GM23280 obtained from the Coriell
543 Institute) using the protocol described by Reinhardt et al[52]. The differentiation protocol from

544 smNPC to neurons involves over-expression of Neurogenin-2 (NGN2) using a modified
545 version of the NGN2 lentiviral inducible vector system (single vector
546 pLV_TRET_hNgn2_UBC_BSD_T2A_rtTA3). The detailed description about protocol,
547 reagents and media composition is available in Dhingra et al.[53].

548 Briefly, stable NGN2 smNPC are grown for six days in expansion medium N2B27
549 supplemented with CHIR99021 (CHIR) 3 μM, Purmorphamine (PMA) 0.5 μM and L-ascorbic
550 acid 2-phosphate magnesium (AA) 64 mg/l. For differentiation, cells are plated (80,000
551 cells/cm2) onto Poly L-orithine and laminin coated plates in N2B27 medium supplemented
552 with doxycycline (dox) at 2.5 μg/mL, and 2 μM DAPT. On day 4 of differentiation,
553 transfection was performed in n=3 replicate plates using lipofectamine RNAiMax
554 (ThermoFisher Scientific) with a final concentration of miRNA mimic and inhibitors (miR-19b-
555 3p and miR-1505p mimics and inhibitors from Qiagen and miR-193a-3p mimic and inhibitor
556 from ThermoFisher Scientific) in the range of 5 to 10 nM as per the manufactures' guidelines
557 along with their corresponding controls. Next day (day 5 of differentiation), the complete
558 media was changed with N2B27 media supplemented with dox, 10 ng/mL brain-derived
559 neurotrophic factor (BDNF), 10 ng/mL glial cell-derived neurotrophic factor (GDNF), 10
560 ng/mL neurotrophic factor 3 (NT-3), 1 μg/mL Laminin, and 10 μM DAPT. Thereafter, half
561 media was changed on day 8 of differentiation. On day 11, cells were gently washed with
562 PBS and processed for RNA isolation.

563

564 *hIPS-derived microglia and miRNA mimics and inhibitors transfection*

565 hiPSCs were differentiated as previously described (van Wilgenburg et al[54]). In brief, 3 x
566 10^6 iPSCs were seeded into an Aggrewell 800 well (STEMCELL Technologies) to form
567 embryoid bodies (EBs), in mTeSR1 and fed daily with medium plus 50ng/ml BMP4 (Miltenyi
568 Biotec), 50ng/ml VEGF (Miltenyi Biotec), and 20ng/ml SCF (R&D Systems). Four-day EBs
569 were then differentiated in 6-well plates (15 EBs/well) in X-VIVO15 (Lonza) supplemented

570 with 100ng/ml M-CSF (Miltenyi Biotec), 25ng/ml IL-3 (Miltenyi Biotec), 2mM Glutamax
571 (Invitrogen Life Technologies), and 0.055mM beta-mercaptoethanol (Thermo Fisher
572 Scientific), with fresh medium added weekly. Microglial precursors emerging in the
573 supernatant after approximately 1 month were collected and isolated through a 40um cell
574 strainer and plated in N2B27 media supplemented with 100 ng/ml M-CSF, 25 ng/ml
575 interleukin 34 (IL-34) for differentiation. Thereafter, the media is reshred every 2 days
576 supplemented with 100 ng/ml M-CSF, and 25 ng/ml IL-34. The cells were cultured for
577 additional 6 days with media refresh every 2 days. On day 7 of maturation, transfection was
578 performed in n=3 replicate plates using lipofectamine RNAiMax with a final concentration of
579 miRNA mimics and inhibitors in the range of 5 to 10 nM as per the manufactures' guidelines
580 along with their corresponding controls (miR-19b-3p and miR-1505p mimics and inhibitors
581 from Qiagen and miR-193a-3p mimic and inhibitor from ThermoFisher Scientific). Next day
582 complete media was refreshed. On day 11, cells were gently washed with PBS and
583 processed for RNA isolation.

584

585 **Genetic analysis**

586 Genomic DNA was isolated from 50 mg of GFM frozen brain tissue by using the Qiamp DNA
587 mini kit (Qiagen) following the manufacturer protocol. DNA concentration and purity were
588 assessed by nanodrop measurement. DNA integrity was evaluated by loading 100
589 nanogram per sample on a 0,8% agarose gel and comparing size distribution to a size
590 standard.

591 Presence of C9orf72-HRE in postmortem brain tissues and hIPS cells was confirmed by
592 primed repeat PCR according to established protocols. Reported mutations for MAPT and
593 GRN were verified by sanger sequencing.

594

595 **Transcriptomic procedures**

596 *RNA isolation from human brain tissue*

597 Total RNA for CAGE-seq and RNAseq was isolated from ±100mg of frozen brain tissue with
598 TRIzol reagent (Thermo Fischer Scientific) according to the manufacturer recommendation,
599 followed by purification with the RNeasy mini columns (Qiagen) after DNAse treatment.

600

601 Total RNA for smallRNA-seq was isolated from frozen tissue using the TRIzol reagent
602 (ThermoFischer Scientific). After isopropanol precipitation and 80% ethanol rinsing RNA
603 pellet was resuspended in RNAse free water and up to 10 micrograms of RNA was
604 incubated with 2U of Ambion DNAse I (ThermoFischer) at 37°C for 20 minutes. DNA-free
605 RNA samples were then further purified by phenol-chloroform-isoamyl-alchol extraction
606 followed by ethanol precipitation.

607

608 *RNA isolation from smNPC-derived neurons and microglia*

609 Total RNA was isolated from NGN2 driven neurons and microglia cells after transfection with
610 miRNA mimics and inhibitors. Briefly at day 11 of transfection cells were carefully rinsed with
611 PBS and lysed in Qiazol buffer (Qiagen). Further DNAse treatment and purification were
612 carried out with the miRNeasy micro kit (Qiagen) according to the manufacturer protocol.

613

614 **RNA QC**

615 For each RNA sample, RNA concentration (A_{260}) and purity ($A_{260/280}$ and $A2_{60/230}$) were
616 determined by Nanodrop measurement and RNA integrity (RIN) was assessed on a
617 Bioanalyser 2100 system and/or Tape station 41200 (Agilent Technologies Inc.)

618

619 *CAGE-seq libraries*

620 CAGE-seq libraries were prepared from 5 micrograms of RNA from frozen brain tissues
621 according to a published protocol[55]. Libraries were sequenced on a HiSeq 2000 and/or
622 HiSeq2500 on a 1x50 bp single read (SR) flow cell (Illumina) at an average of 20M
623 reads/sample.

624

625 *RNAseq libraries*

626 Total RNAseq libraries were prepared from 1 microgram of total RNA from frozen brain
627 tissue using the TruSeq Stranded Total RNA with Ribo-Zero Gold kit (Illumina) according to
628 the protocol specifications. RNAseq libraries were sequenced on a Hiseq2500 and
629 HISeq4000 on a 2x100 bp paired end (PE) flow cell (Illumina) at an average of 100M
630 PE/sample.

631

632 *smallRNAseq libraries*

633 Small RNA-seq libraries were prepared from 1 microgram of total RNA from NPC-derived
634 neurons and 300 nanograms of microglia after miRNA mimics and inhibitors transfection,
635 using the mRNA TrueSeq Stranded kit (Illumina). mRNAseq libraries were sequenced on a
636 NextGen550 on a 75 cycles flow cell (Illumina). Small RNAseq libraries from frozen tissue
637 were prepared starting from 2 micrograms of total RNA using the Nextflex Small RNA-seq kit
638 v3 (Bioo Scientific) and the NEBNext Small RNA library prep set for Illumina (New England
639 Biolabs). Libraries were sequenced on a NextSeq550 on a 75 cycles flow cell.

640

641

642 **Methylation assay**

643 To assess the methylation status of over 850000 CpG sites in promoter, gene body and
644 enhancer regions we have used the MethylationEPIC bead chip arrays (Illumina).

645 Bisulfite conversion of genomic DNA, genome amplification, hybridization to the beadchips,
646 washing, staining and scanning procedure was performed by Atlas Biolabs (Atlas Biolabs,
647 Berlin, Germany). Cases and controls DNAs were distributed randomly across each array.

648

649 **HumanBase Module Analysis**

650 Functional gene modules were generated using the HumanBase tool at:
651 https://hb.flatironinstitute.org/. We divided DEGs into up- and down-regulated genes as we
652 were looking for active and repressed modules in FTD. Modules were downloaded for further
653 analysis. Cell type enrichment analysis was performed for genes of each modules using
654 EWCE[56] as described further down.

655 **RNA-seq processing and analysis**

656 Raw FastQ files were processed using the RNA-seq pipeline from nf-core (nf-core/rnaseq
657 v1.3) [57], with trimming enabled. Gene quantification was subsequently done using Salmon
658 (v0.14.1)[58] on the trimmed FastQ files. Alignment and mapping were performed against the
659 human genome hg38. DESeq2 (v.1.26.0)[59] was used to perform differential expression
660 analysis. We corrected for the covariates gender and PH-value. Genes were considered
661 differentially expressed when having a Benjamini-Hochberg corrected P-value below 0.05.

662 **Cell type deconvolution and filtering**

663 We performed cell type deconvolution on the RNA-seq data using Scaden[60]. For training we
664 used the human brain training dataset used in the Scaden publication. Each ensembl model
665 was trained for 5000 steps. To filter differentially expressed genes for false positives caused
666 by cell composition bias, we first calculated the correlation of gene expression with cell type
667 fraction. Then, we calculated a cell type specificity score as defined in Skene et al. [56] for

668 each gene available in the scRNA-seq dataset from Darmanis et al. [61]. We filtered out all
669 genes that had a specificity score of at least 0.5 and a positive correlation of at least 0.4 with
670 the cell type fractions of the most specific cell type. False positive DEGs that are caused by
671 systematic increase or decrease of a specific cell type will show high correlation with the cell
672 type fractions and can thus be identified and removed from the analysis. A specificity score
673 of 0.5 means that half of the total gene expression for a certain gene can be attributed to a
674 single cell type, assuming a uniform cell type composition. The cut-offs for specificity score
675 and correlation were chosen based on an informed decision. Relative changes in cell type
676 composition were quantified by first calculating the average fractions of a cell type for all
677 groups and then calculating the percentual change of cell fractions compared to the average
678 control fractions. This allows to detect relative changes in cell type compositions. Statistical
679 significance between cell type fractions of groups was assessed using a t-test in the R
680 language.

681 **Cell type enrichment analysis**

682 We performed cell type enrichment analysis of genesets using the EWCE R package[56]. Cell
683 type specificity of genes was calculated from the single-cell RNA-seq cortex dataset of
684 Darmanis and colleagues[61]. EWCE analysis was done following instructions from
685 https://github.com/NathanSkene/EWCE.

686 **CAGE-seq processing and analysis**

687 Sequencing adapters and barcodes in CAGE-seq FastQ files were trimmed using Skewer
688 (v.0.1.126)[62]. Sequencing artefacts were removed using TagDust (v1.0)[63]. Processed reads
689 were then aligned against the human genome hg38 using STAR (v.2.4.1)[64]. CAGE detected
690 TSS (CTSS) files were created using CAGEr (v1.10.0)[65]. With CAGEr, we removed the first
691 G nucleotide if it was a mismatch. CTSS were clustered using the 'distclu' method with a
692 maximum distance of 20 bp. For exact commands used we refer to the reader to the scripts
693 used in this pipeline: https://github.com/dznetubingen/cageseq-pipeline-mf.

694 **Transcription factor activity analysis**

695 To identify candidate regulatory transcription factors, we first performed differential
696 expression analysis with all CAGE-seq clusters (see RNA-seq analysis). Then, we extracted
697 the sequence 600 bp up-stream and 300 bp downstream around all detected clusters. We
698 used Homer[66] to look for significant TFBS enrichment in the regions around up- and down-
699 regulated clusters (similar to [67]). TFBS motifs were downloaded from the JASPAR
700 database[68]. When calculating enrichment, we considered all extracted regions that are not
701 part of the set of interest as background. The complete pipeline can be found at
702 https://github.com/KevinMenden/tf-activity. We selected all TFs with significant enrichment
703 (p-value <= 0.001) for either up-regulated or down-regulated CAGE clusters as candidate
704 regulators. We considered genes as potential targets of a TF if a TFBS could be found in
705 their promoter region. As an additional filter, we selected only TFs with evidence for
706 differential expression in the RNA-seq data (adj. P-value < 0.05, not filtered for cell
707 composition).

708 **smRNA-seq processing and analysis**

709 After removing sequencing adapters, all FastQ files were uploaded to OASIS2 [69] for
710 analysis. Subsequent differential expression analysis was performed on the counts yielded
711 from OASIS2, using DESeq2 and correcting for gender and PH-value, as was done for the
712 RNA-seq data. Additionally, we added a batch variable to the design matrix to correct for the
713 two different batches of this dataset. For the target prediction analysis, we first downloaded
714 all targets from mirBase[70]. Then, we correlated the expression of miRNAs with their
715 predicted targets using matching samples from the RNA-seq data. We removed all predicted
716 targets with a correlation above -0.4, thus only considering miRNA-target pairings with high
717 negative correlation.

718

719 **Methylation data processing and analysis**

720 The Infinium MethylationEPIC BeadChip data was analyzed using the minfi R package[71]. We

721 removed all sites with a detection P-value above 0.01, on sex chromosomes and with single
722 nucleotide polymorphisms (SNPs). Data normalization was done using stratified quantile
723 normalization. Sites with a standard deviation below 0.1 were considered uninformative and
724 filtered out, to increase detection power. Surrogate variable analysis[72] was performed to
725 determine confounding factors. Differential methylation analysis was done using the limma
726 package[73] and controlling for the detected surrogate variables. Sites with a Benjamini-
727 Hochberg [74] adjusted P-value below 0.05 were considered differentially methylated.

728 **Age prediction**

729 We predicted the biological age of donors using the methylation data and the Wenda
730 algorithm[75]. Training data was kindly provided by the authors of Wenda. We subsetted the
731 data for CpG sites found in our data (11,729) sites and performed the prediction as
732 described at https://github.com/PfeiferLabTue/wenda.

733

734 **Analysis of mRNA-seq data from cellular models**

735 This section describes the analysis of mRNA-seq data generated for the miRNA mimic and
736 inhibitor experiments. FastQ files were mapped and gene counts quantified using Salmon
737 and differential expression analysis was performed with DESeq2 (see post-mortem brain
738 RNA-seq analysis). DEGs were examined for pathway enrichment using go:Profiler.

739

740 **Assessment of degeneration**

741 For assessment of neurodegeneration, H&E stained paraffin sections of the frontal and
742 temporal cortex were graded as absent (0), mild (1), moderate (2) and severe (3) based on
743 the presence of spongiosis, neuronal loss and gliosis.

744

745 # Data Availability

746 All data used in this study and published as phase 1 of the RiMod-FTD resource have been
747 deposited at the European Phenome-genome Archive (EGA) under accession number
748 EGAS00001004895.

749 # Code Availability

750 The code used for generating the analysis results is made freely available in the GitHub
751 repository https://github.com/dznetubingen/rimod-ftd-paper.

752 # References

753 1. Bang, J., Spina, S. & Miller, B. L. Frontotemporal dementia. *Lancet* **386**, 1672–1682
754 (2015).

755 2. Panza, F. *et al.* Development of disease-modifying drugs for frontotemporal dementia
756 spectrum disorders. *Nat. Rev. Neurol.* **16**, 213–228 (2020).

757 3. Seelaar, H., Rohrer, J. D., Pijnenburg, Y. A. L., Fox, N. C. & van Swieten, J. C.
758 Clinical, genetic and pathological heterogeneity of frontotemporal dementia: a review.
759 *J. Neurol. Neurosurg. Psychiatry* **82**, 476–486 (2011).

760 4. Olszewska, D. A., Lonergan, R., Fallon, E. M. & Lynch, T. Genetics of Frontotemporal
761 Dementia. *Current Neurology and Neuroscience Reports* vol. 16 (2016).

762 5. Sirkis, D. W., Geier, E. G., Bonham, L. W., Karch, C. M. & Yokoyama, J. S. Recent
763 Advances in the Genetics of Frontotemporal Dementia. *Curr. Genet. Med. Rep.* **7**, 41–
764 52 (2019).

765 6. Sieben, A. *et al.* The genetics and neuropathology of frontotemporal lobar
766 degeneration. *Acta Neuropathologica* vol. 124 353–372 (2012).

767 7. Balendra, R. & Isaacs, A. M. C9orf72-mediated ALS and FTD: multiple pathways to
768 disease. *Nat. Rev. Neurol.* 1 (2018) doi:10.1038/s41582-018-0047-2.

769 8. RiMod-FTD | JPND. https://www.neurodegenerationresearch.eu/initiatives/annual-
770 calls-for-proposals/closed-calls/risk-factors-2012/risk-factor-call-results/rimod-ftd/.

771 9. Raudvere, U. *et al.* g:Profiler: a web server for functional enrichment analysis and
772 conversions of gene lists (2019 update). *Nucleic Acids Res.* **47**, W191–W198 (2019).

773 10. Golpich, M. *et al.* Mitochondrial Dysfunction and Biogenesis in Neurodegenerative
774 diseases: Pathogenesis and Treatment. *CNS Neurosci. Ther.* **23**, 5–22 (2017).

775 11. Li, Y., Li, Z.-X., Jin, T., Wang, Z.-Y. & Zhao, P. Tau Pathology Promotes the
776 Reorganization of the Extracellular Matrix and Inhibits the Formation of Perineuronal
777 Nets by Regulating the Expression and the Distribution of Hyaluronic Acid Synthases.

J. Alzheimer's Dis. **57**, 395–409 (2017).

12. Végh, M. J. *et al.* Reducing hippocampal extracellular matrix reverses early memory deficits in a mouse model of Alzheimer's disease. *Acta Neuropathol. Commun.* **2**, (2014).

13. Lu, P., Takai, K., Weaver, V. M. & Werb, Z. Extracellular Matrix degradation and remodeling in development and disease. *Cold Spring Harb. Perspect. Biol.* **3**, (2011).

14. Duits, F. H. *et al.* Matrix Metalloproteinases in Alzheimer's Disease and Concurrent Cerebral Microbleeds. *J. Alzheimer's Dis.* **48**, 711–720 (2015).

15. Xi, Z. *et al.* Hypermethylation of the CpG Island Near the G 4 C 2 Repeat in ALS with a C9orf72 Expansion. *Am J Hum Genet* 981–989 (2013) doi:10.1016/j.ajhg.2013.04.017.

16. Biswas, M. H. U. *et al.* MMP-9 and MMP-2 Contribute to Neuronal Cell Death in iPSC Models of Frontotemporal Dementia with MAPT Mutations. *Stem Cell Reports* **7**, 316–324 (2016).

17. Young, J. J., Lavakumar, M., Tampi, D., Balachandran, S. & Tampi, R. R. Frontotemporal dementia: latest evidence and clinical implications. *Ther. Adv. Psychopharmacol.* **8**, 33–48 (2018).

18. Cash, D. M. *et al.* Patterns of gray matter atrophy in genetic frontotemporal dementia: results from the GENFI study. *Neurobiol. Aging* **62**, 191–196 (2018).

19. Fu, H., Hardy, J. & Duff, K. E. Selective vulnerability in neurodegenerative diseases. *Nat. Neurosci.* **21**, 1350–1358 (2018).

20. Palese, F. *et al.* Anti-GluA3 antibodies in frontotemporal dementia: effects on glutamatergic neurotransmission and synaptic failure. *Neurobiol. Aging* **86**, 143–155 (2020).

21. Murley, A. G. & Rowe, J. B. Neurotransmitter deficits from fronto temporal lobar degeneration. *Brain* **141**, 1263–1285 (2018).

22. Bennett, R. E. *et al.* Tau induces blood vessel abnormalities and angiogenesis-related gene expression in P301L transgenic mice and human Alzheimer's disease. *Proc. Natl. Acad. Sci. U. S. A.* **115**, E1289–E1298 (2018).

23. Ek Olofsson, H. & Englund, E. A cortical microvascular structure in vascular dementia, Alzheimer's disease, frontotemporal lobar degeneration and nondemented controls: a sign of angiogenesis due to brain ischaemia? *Neuropathol. Appl. Neurobiol.* **45**, 557–569 (2019).

24. Park, L. *et al.* Tau induces PSD95–neuronal NOS uncoupling and neurovascular dysfunction independent of neurodegeneration. *Nat. Neurosci.* **23**, 1079–1089 (2020).

25. Greene, C. S. *et al.* Understanding multicellular function and disease with human tissue-specific networks. *Nat. Genet.* **47**, 569–576 (2015).

26. Skene, N. G. & Grant, S. G. N. Identification of Vulnerable Cell Types in Major Brain Disorders Using Single Cell Transcriptomes and Expression Weighted Cell Type Enrichment. *Front. Neurosci.* **10**, 16 (2016).

27. Paushter, D. H., Du, H., Feng, T. & Hu, F. The lysosomal function of progranulin, a guardian against neurodegeneration. *Acta Neuropathol.* **136**, 1 (2018).

28. Lui, H. *et al.* Progranulin Deficiency Promotes Circuit-Specific Synaptic Pruning by Microglia via Complement Activation. *Cell* **165**, 921–935 (2016).

822 29. Krabbe, G. *et al.* Microglial NFκB-TNFα hyperactivation induces obsessive-
823 compulsive behavior in mouse models of progranulin-deficient Frontotemporal
824 dementia. *Proc. Natl. Acad. Sci. U. S. A.* **114**, 5029–5034 (2017).

825 30. Martens, L. H. *et al.* Progranulin deficiency promotes neuroinflammation and neuron
826 loss following toxin-induced injury. *J. Clin. Invest.* **122**, 3955–3959 (2012).

827 31. Zou, M. *et al.* Autophagy inhibition of hsa-miR-19a-3p/19b-3p by targeting TGF-β R II
828 during TGF-β1-induced fibrogenesis in human cardiac fibroblasts. *Sci. Rep.* **6**, 1–15
829 (2016).

830 32. Whitwell, J. L. *et al.* Neuroimaging signatures of frontotemporal dementia genetics:
831 C9ORF72, tau, progranulin and sporadics. *Brain* **135**, 794–806 (2012).

832 33. Benussi, A. *et al.* Toward a glutamate hypothesis of frontotemporal dementia. *Front.*
833 *Neurosci.* **13**, (2019).

834 34. Zhang, J. *et al.* Neurotoxic microglia promote TDP-43 proteinopathy in progranulin
835 deficiency. *Nature* (2020) doi:10.1038/s41586-020-2709-7.

836 35. Woollacott, I. O. C. & Rohrer, J. D. The clinical spectrum of sporadic and familial
837 forms of frontotemporal dementia. *J. Neurochem.* **138**, 6–31 (2016).

838 36. Sakae, N. *et al.* Microglia in frontotemporal lobar degeneration with progranulin or
839 C9ORF72 mutations. *Ann. Clin. Transl. Neurol.* **6**, 1782–1796 (2019).

840 37. Yuan, J., Amin, P. & Ofengeim, D. Necroptosis and RIPK1-mediated
841 neuroinflammation in CNS diseases. *Nat. Rev. Neurosci.* **20**, 19–33 (2019).

842 38. Xu, D. *et al.* TBK1 Suppresses RIPK1-Driven Apoptosis and Inflammation during
843 Development and in Aging. *Cell* **174**, 1477-1491.e19 (2018).

844 39. Molnár, T. *et al.* Current translational potential and underlying molecular mechanisms
845 of necroptosis. *Cell Death Dis.* **10**, 1–21 (2019).

846 40. Brkic, M., Balusu, S., Libert, C. & Vandenbroucke, R. E. Friends or Foes: Matrix
847 Metalloproteinases and Their Multifaceted Roles in Neurodegenerative Diseases.
848 *Mediators Inflamm.* **2015**, (2015).

849 41. Rivera, S., García-González, L., Khrestchatisky, M. & Baranger, K. Metalloproteinases
850 and their tissue inhibitors in Alzheimer's disease and other neurodegenerative
851 disorders. *Cell. Mol. Life Sci.* **76**, 3167–3191 (2019).

852 42. Kiaei, M. *et al.* Matrix metalloproteinase-9 regulates TNF-α and FasL expression in
853 neuronal, glial cells and its absence extends life in a transgenic mouse model of
854 amyotrophic lateral sclerosis. *Exp. Neurol.* **205**, 74–81 (2007).

855 43. Lorenzl, S. *et al.* The matrix metalloproteinases inhibitor Ro 26-2853 extends survival
856 in transgenic ALS mice. *Exp. Neurol.* **200**, 166–171 (2006).

857 44. Lee, J. K. *et al.* Tissue inhibitor of metalloproteinases-3 (TIMP-3) expression is
858 increased during serum deprivation-induced neuronal apoptosis in vitro and in the
859 G93A mouse model of amyotrophic lateral sclerosis: A potential modulator of Fas-
860 mediated apoptosis. *Neurobiol. Dis.* **30**, 174–185 (2008).

861 45. Vandenbroucke, R. E. *et al.* Matrix metalloproteinase 13 modulates intestinal
862 epithelial barrier integrity in inflammatory diseases by activating TNF. *EMBO Mol.*
863 *Med.* **5**, 1000–1016 (2013).

864 46. Rempe, R. G., Hartz, A. M. S. & Bauer, B. Matrix metalloproteinases in the brain and
865 blood-brain barrier: Versatile breakers and makers. *J. Cereb. Blood Flow Metab.* **36**,

866 1481–1507 (2016).

867 47. Woo, M. S., Park, J. S., Choi, I. Y., Kimf, W. K. & Kim, H. S. Inhibition of MMP-3 or -9
868 suppresses lipopolysaccharide-induced expression of proinflammatory cytokines and
869 iNOS in microglia. *J. Neurochem.* **106**, 770–780 (2008).

870 48. Garcia-Alloza, M. *et al.* Matrix metalloproteinase inhibition reduces oxidative stress
871 associated with cerebral amyloid angiopathy in vivo in transgenic mice. *J. Neurochem.*
872 **109**, 1636–1647 (2009).

873 49. Aoki, Y. *et al.* C9orf72 and RAB7L1 regulate vesicle trafficking in amyotrophic lateral
874 sclerosis and frontotemporal dementia. *Brain* 887–897 (2017)
875 doi:10.1093/brain/awx024.

876 50. Yarwood, R., Hellicar, J., Woodman, P. G. & Lowe, M. Membrane trafficking in health
877 and disease. *DMM Dis. Model. Mech.* **13**, (2020).

878 51. Wren, M. C. *et al.* Frontotemporal dementia-associated N279K tau mutant disrupts
879 subcellular vesicle trafficking and induces cellular stress in iPSC-derived neural stem
880 cells. *Mol. Neurodegener.* **10**, 46 (2015).

881 52. Reinhardt, P., Glatza, M., Hemmer, K., Tsytsyura, Y. & Thiel, C. S. Derivation and
882 Expansion Using Only Small Molecules of Human Neural Progenitors for
883 Neurodegenerative Disease Modeling. *PLoS One* **8**, 59252 (2013).

884 53. Dhingra, A. *et al.* Automated production of human induced pluripotent stem cell-
885 derived cortical and dopaminergic neurons with integrated live-cell monitoring. *J. Vis.*
886 *Exp.* **2020**, 1–29 (2020).

887 54. van Wilgenburg, B., Browne, C., Vowles, J. & Cowley, S. A. Efficient, Long Term
888 Production of Monocyte-Derived Macrophages from Human Pluripotent Stem Cells
889 under Partly-Defined and Fully-Defined Conditions. *PLoS One* **8**, (2013).

890 55. Takahashi, H., Lassmann, T., Murata, M. & Carninci, P. 5′ end–centered expression
891 profiling using cap-analysis gene expression and next-generation sequencing. *Nat.*
892 *Protoc.* **7**, 542–561 (2012).

893 56. Skene, N. G. & Grant, S. G. N. Identification of Vulnerable Cell Types in Major Brain
894 Disorders Using Single Cell Transcriptomes and Expression Weighted Cell Type
895 Enrichment. *Front. Neurosci.* **10**, 16 (2016).

896 57. Ewels, P., Magnusson, M., Lundin, S. & Käller, M. MultiQC: Summarize analysis
897 results for multiple tools and samples in a single report. *Bioinformatics* **32**, 3047–3048
898 (2016).

899 58. Patro, R., Duggal, G., Love, M. I., Irizarry, R. A. & Kingsford, C. Salmon provides fast
900 and bias-aware quantification of transcript expression. *Nat. Publ. Gr.* **14**, (2017).

901 59. Love, M. I., Huber, W. & Anders, S. Moderated estimation of fold change and
902 dispersion for RNA-seq data with DESeq2. *Genome Biol.* **15**, (2014).

903 60. Menden, K. *et al.* Deep learning–based cell composition analysis from tissue
904 expression profiles. *Sci. Adv.* **6**, eaba2619 (2020).

905 61. Darmanis, S. *et al.* A survey of human brain transcriptome diversity at the single cell
906 level. *Proc. Natl. Acad. Sci. U. S. A.* **112**, 7285–7290 (2015).

907 62. Jiang, H., Lei, R., Ding, S. W. & Zhu, S. Skewer: A fast and accurate adapter trimmer
908 for next-generation sequencing paired-end reads. *BMC Bioinformatics* **15**, 182 (2014).

909 63. Lassmann, T. TagDust2: A generic method to extract reads from sequencing data.

910 *BMC Bioinformatics* **16**, 24 (2015).

911 64. Dobin, A. & Gingeras, T. R. Mapping RNA-seq Reads with STAR. in *Current Protocols*
912 *in Bioinformatics* (2015). doi:10.1002/0471250953.bi1114s51.

913 65. Haberle, V., Forrest, A. R. R., Hayashizaki, Y., Carninci, P. & Lenhard, B. CAGEr:
914 Precise TSS data retrieval and high-resolution promoterome mining for integrative
915 analyses. *Nucleic Acids Res.* **43**, e51–e51 (2015).

916 66. Heinz, S. *et al.* Simple Combinations of Lineage-Determining Transcription Factors
917 Prime cis-Regulatory Elements Required for Macrophage and B Cell Identities. *Mol.*
918 *Cell* **38**, 576–589 (2010).

919 67. Arenillas, D. J. *et al.* CAGEd-oPOSSUM: motif enrichment analysis from CAGE-
920 derived TSSs. *Bioinformatics* **32**, 2858–60 (2016).

921 68. Khan, A. *et al.* JASPAR 2018: update of the open-access database of transcription
922 factor binding profiles and its web framework. *Nucleic Acids Res.* **46**, D260–D266
923 (2018).

924 69. Rahman, R. U. *et al.* Oasis 2: Improved online analysis of small RNA-seq data. *BMC*
925 *Bioinformatics* **19**, 54 (2018).

926 70. Kozomara, A., Birgaoanu, M. & Griffiths-Jones, S. MiRBase: From microRNA
927 sequences to function. *Nucleic Acids Res.* **47**, D155–D162 (2019).

928 71. Aryee, M. J. *et al.* Minfi: A flexible and comprehensive Bioconductor package for the
929 analysis of Infinium DNA methylation microarrays. *Bioinformatics* **30**, 1363–1369
930 (2014).

931 72. Leek, J. T. & Storey, J. D. Capturing Heterogeneity in Gene Expression Studies by
932 Surrogate Variable Analysis. *PLoS Genet.* **3**, e161 (2007).

933 73. Ritchie, M. E. *et al.* limma powers differential expression analyses for RNA-
934 sequencing and microarray studies. *Nucleic Acids Res.* (2015)
935 doi:10.1093/nar/gkv007.

936 74. Benjamini, Y. & Hochberg, Y. Controling the False Discovery Rate: A Practical and
937 Powerful Approach to Multiple Testing. *J. R. Stat. Soc.* (1995).

938 75. Handl, L., Jalali, A., Scherer, M., Eggeling, R. & Pfeifer, N. Weighted elastic net for
939 unsupervised domain adaptation with application to age prediction from DNA
940 methylation data. in *Bioinformatics* vol. 35 i154–i163 (Oxford University Press, 2019).

941

942

943

944

Acknowledgements

Post-mortem brain tissue was obtained from the Dutch Brain Bank, Netherlands Institute for Neuroscience, Amsterdam, and from the London Neurodegenerative Disease Brain Bank, King's College London, London, UK. The London Neurodegenerative Disease Brain Bank is part of the Brains for Dementia Research Initiative.

Author contributions

The project was initiated and designed by PH. Small RNA-seq experiments were performed by AF, LK, PR and NF. RNA-seq and CAGE-seq experiments were performed by CB, PR, NF, MC. iPSC-derived neuron and microglia experiments were performed by AD and DKV.

Analysis of CAGE-seq data was done by MF, TN and KM. JSS, BA and KM analysed the RNA-seq data. KM analysed the smRNA-seq and methylation data. PH, SB, PR planned and interpreted all performed analyses. KM, PH, PR and SB wrote the manuscript.

Funding

This work was funded in part by the EU Joint Programme - Neurodegenerative Disease Research (JPND) project: Risk and Modifying factors for FTD (RiMod-FTD), NOMIS Foundation and BMBF IDSN. DKV is in receipt of an Alexander von Humboldt Research Fellowship.

RiMod-FTD Partners

Prof. Dr. P. Heutink: Kevin Menden; Margherita Francescatto; Tenzin Nyima; Cornelis Blauwendraat; Burcu Atarsu; Javier Simon Sanchez; Stefan Bonn; Patrizia Rizzu;

German Center for Neurodegenerative Diseases (DZNE)-Tübingen

Otfried Müller Strasse 23

967 72076 Tübingen

968 Germany

969 Tel.: +49 (0)7071 9254 050

970 E-Mail: peter.heutink@dzne.de

971

972 Prof. Dr. J. Hardy:

973 Reta Lila Weston Research Laboratories, Dept. of

974 Molecular Neuroscience, UCL Institute of

975 Neurology, London WC1N 3BG, England.

976 Tel: +44 (0) 207 679 4297.

977 E-Mail: j.hardy@UCL.AC.UK

978

979 Prof. Dr. A. Brice

980 Research Centre of the Brain and Spine Institute

981 (CRicm UMR_S975), Pitié-Salpêtrière Hospital, 47

982 boulevard de l'Hôpital, 75013 Paris, France

983 Tel: +33 1 572746 82

984 E-Mail: alexis.brice@upmc.fr

985

986 Prof. Dr. J.C. van Swieten; Fenne Riemslagh

987 Prof. Dr. A.B. Smit: Pim van Nierop; Suzanne Miedema

988 Dept. Neurology, ErasmusMC, ‘s-Gravendijkwal 230

989 3015 CE Rotterdam, Netherlands.

990 Tel: +31 107033274

991 E-Mail: j.c.vanswieten@erasmusmc.nl

992

993 Prof. Dr. P. Longone/

994 Prof. Dr. E. Buratti/

995 Prof. Dr. A. Alberici

996 Molecular Neurobiology Unit

997 Santa Lucia Foundation

998 Via del Fosso di Fiorano 64

999 00179 Roma Italia

1000 Tel. +39-06501703151

1001 E-Mail: p.longone@hsnatalucia.it

1002

1003 Prof. Dr. P. van Damme

1004 Laboratory for Neurobiology (Vesalius Research

1005 Center) O&N IV Herestraat 49 - bus 912.

1006 3000 Leuven, Belgium

1007 Tel. +32 16 3 73181

1008 E-Mail: philip.vandamme@vib-kuleuven.be

Dr. A. Sandelin

Department of Biology, Copenhagen University,

Ole Maaoles vej 5,

DK2200 Copenhagen, Denmark.

Tel +45 35321285/ Email: albin@binf.ku.dk

Prof. Dr. A. Fischer

Dept. of Psychiatry and Psychotherapy, University

of Göttingen, German Center for Neurodegenerative

Diseases (DZNE) Göttingen, Grisebach Str. 5,

37077 Göttingen, Germany.

Tel: +49 551 30178.

E-Mail: afische2@gwdg.de

Prof. Dr. S. Lichtenthaler

Technical University Munich (TUM) and German

Center for Neurodegenerative Diseases (DZNE),

Max-Lebsche Platz 30, 81377 Munich, Germany.

Tel: +49 89 7095 8405

E-Mail: stefanlichtethaler@dzne.de

Prof. Dr. E. Mandelkow + Prof. Dr. E. Mandelkow + Marta Anglada

German Center for Neurodegenerative Diseases

(DZNE), Ludwig-Erhard-Allee 2 53175 Bonn,

Germany.

Tel: +49 (0) 228 / 43302-630

E-Mail: eckhard.mandelkow@dzne.de

Competing Interests

The authors declare no competing interests.